Int.J. Applied Thermodynamics, **ISSN 1301-9724**
Vol.2 (No.4), pp.145-157, December-1999

Entropy Generation Minimization in a Ram-Air Cross-Flow Heat Exchanger

Asad ALEBRAHIM and Adrian BEJAN
Department of Mechanical Engineering and Materials Science
Box 90300, Duke University, Durham, NC 27708-0300 – USA
E-mail: abejan@duke.edu

Abstract

This paper presents the constrained thermodynamic optimization of a crossflow heat exchanger with ram air on the cold side. The ram-air stream passes through a diffuser before entering the heat exchanger, and exits through a nozzle. This configuration is used in the environmental control systems of aircraft. In the first part of the study the heat exchanger is optimized alone, subject to fixed total volume and volume fraction occupied by solid walls. Optimized geometric features such as the ratio of channel spacings and flow lengths are reported. It is found that the optimized features are relatively insensitive to changes in other physical parameters of the installation. In the second part of the study the entropy generation rate also accounts for the irreversibility due to discharging the ram-air stream into the atmosphere. The optimized geometric features are relatively insensitive to this additional effect, emphasizing the robustness of the thermodynamic optimum.

Keywords: entropy generation minimization, EGM, thermodynamic optimization

1. Thermodynamic Optimization of Air-Craft Energy Systems

In a paper at the 1999 ASME congress I drew attention to a very important and growing industrial sector that is an ideal candidate for the application of exergy analysis and thermodynamic optimization: energy systems for modern aircraft (Bejan, 1999). Interest is expressed by aircraft manufacturers, government sponsors and university researchers.

Exergy analysis and the minimization of exergy destruction can be used by themselves especially in areas where the total cost of the installation is dominated by the cost due to thermodynamic irreversibility. The classical example of this kind is cryogenics, or refrigeration at very low temperatures, where the power requirement is substantial and proportional to the entropy generated in the cold space (Ahern, 1980; Bejan, 1982).

To see why aircraft energy systems can also be conceptualized on the basis of thermodynamic optimization, consider their objectives and physical constraints. Power and refrigeration systems are assemblies of streams and hardware (components). The size of the hardware is always constrained (e.g., weight, volume). Each stream carries exergy (useful work content), which is the life blood of the power system, i.e., another form of the fuel brought on board and burned in order to drive the system. Exergy is destroyed (or entropy is generated) whenever streams interact with each other and with components. The design objectives are: (i) to optimize streams and components so that they destroy least exergy subject to constraints, and (ii) to make sure that the optimized entities "match", or can be "fitted" together (wrapped around each other) into a new integrative design of the larger system.

What emerges is a visible structure that reflects the optimization principle and the various constraints. The same principle generates geometric shape and structure in natural systems, animate and inanimate, cf. constructal theory (Bejan, 1997, chapter 13).

In an earlier paper in this journal we illustrated this optimization principle by using as example a combined power and refrigeration system driven by a stream of hot gas (Ordoñez et al., 1999). In the present paper we treat the more specific example of a crossflow heat exchanger with a stream of ram air on the cold side. This heat exchanger type is often used in the environmental control system of modern aircraft.

2. Thermodynamic Analysis

The crossflow heat exchanger brings together the hot air stream $\dot{m}_e$ (fixed) drawn from the engine, and the cold ram-air stream $\dot{m}_a$, *Figure 1*. The inlet properties of the two streams are fixed, namely T_e and P_e for the engine stream, and T_a, P_a and V_a for the ram air. The ram air velocity V_a is first decreased in a diffuser such that the inlet to the heat exchanger is characterized by T_1, P_1 and V_1. Immediately downstream of the heat exchanger, the ram air properties are T_2, P_2 and V_2. The stream is accelerated in a nozzle so that the exit pressure drops to the ambient level (P_a), where the velocity (V_2) is comparable with the inlet velocity (V_1). Finally, the exhaust is brought in complete thermal and mechanical equilibrium with the ambient, at state (a).

The rate of entropy generation in the entire system shown with dashed line in *Figure 1* is (Bejan, 1982, 1996; Moran, 1982)

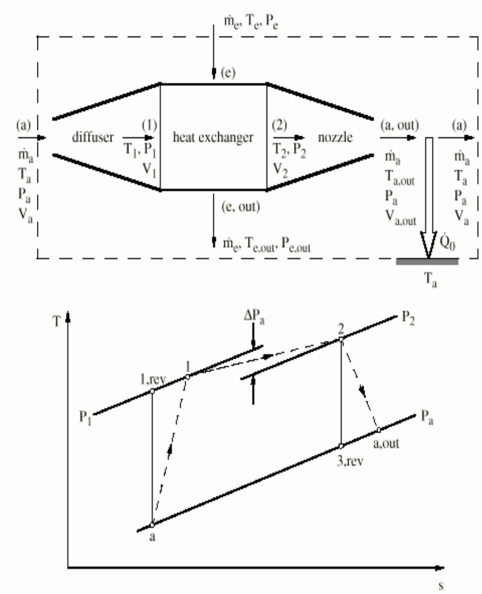

Figure 1. Cross-flow heat exchanger with engine air on the hot side and ram air on the cold side, and the temperature-entropy diagram of the process undergone by the ram air stream.

$$\dot{S}_{gen} = \dot{m}_e\left(c_{pe}\ln\frac{T_{e,out}}{T_e} - R_e\ln\frac{P_{e,out}}{P_e}\right) + \dot{m}_a\left(c_{pa}\ln\frac{T_a}{T_a} - R_a\ln\frac{P_a}{P_a}\right) + \frac{\dot{Q}_0}{T_a} \quad (1)$$

where the term multiplied by $\dot{m}_a$ is zero and

$$\dot{Q}_0 = \dot{m}_a\left[c_{pa}\left(T_{a,out} - T_a\right) + \left(V_{a,out}^2 - V_a^2\right)/2\right].$$

The two fluids are treated as ideal gases with constant specific heats. We expect the larger capacity flow rate to reside on the ram air side,

$$C_{max} = \dot{m}_a c_{pa}\,;\; C_{min} = \dot{m}_e c_{pe}\,;\; \mu = \frac{\dot{m}_a c_{pa}}{\dot{m}_e c_{pe}} > 1 \quad (2)$$

and use C_{min} to nondimensionalize Eq.(1). We also use the ambient properties to nondimensionalize all the temperatures and pressures that appear in this analysis,

$$\tilde{T} = \frac{T}{T_a} \qquad \tilde{P} = \frac{P}{P_a} \quad (3)$$

In this new notation, Eq.(1) delivers the entropy generation number N_S

$$N_S = \frac{\dot{S}_{gen}}{\dot{m}_e c_{pe}} = \ln\frac{\tilde{T}_{e,out}}{\tilde{T}_e} - b_e\ln\frac{\tilde{P}_{e,out}}{\tilde{P}_e} + \mu\left(\tilde{T}_{a,out} - 1 + \frac{V_{a,out}^2 - V_a^2}{2c_{pa}T_a}\right) \quad (4)$$

where $b_e = (R/c_p)_e$ and $b_a = (R/c_p)_a$ are known constants. Fixed parameters are $\tilde{T}_e$ and $\tilde{P}_e$, while μ, $\tilde{T}_{a,out}$, $\tilde{T}_{e,out}$ and $\tilde{P}_{e,out}$ may vary. Included in the calculated N_S are the irreversibilities of the diffuser, heat exchanger, nozzle and mixing of the exhaust with the ambient.

The variable parameters are related through the first law statements for the three physical components that appear in *Figure 1*. The diffuser (a) $\rightarrow$ (1) is governed by the first law (Moran and Shapiro, 1995),

$$c_{pa}\left(T_1 - T_a\right) = \frac{1}{2}\left(V_a^2 - V_1^2\right) \quad (5)$$

The state (1) is determined with reference to the temperature-entropy diagram of *Figure 1*, by specifying the diffuser isentropic efficiency

$$\eta_d = \frac{c_{pa}\left(T_{1,rev} - T_a\right)}{c_{pa}\left(T_1 - T_a\right)} \lesssim 1 \quad (6)$$

The state (1, rev) is located by intersecting $P_{1,rev} = P_1$ with $s_{1,rev} = s_a$, which yields

$$0 = c_{pa}\ln\frac{T_{1,rev}}{T_a} - R_a\ln\frac{P_{1,rev}}{P_a} \quad (7)$$

The dimensionless version of Eqs.(5)-(7) is

$$\tilde{T}_1 - 1 = \frac{1}{2}\left(v_a^2 - v_1^2\right) \quad (8)$$

$$\tilde{T}_1 - 1 = \frac{1}{\eta_d}\left(\tilde{P}_1^{b_a} - 1\right) \quad (9)$$

where the velocities have been nondimensionalized by defining

$$v = \frac{V}{(c_{pa}T_a)^{1/2}} = M\left(\frac{b_a}{1-b_a}\right)^{1/2} \quad (10)$$

Note that the v definition is comparable with the Mach number definition, $M = V/(k_aR_aT_a)^{1/2}$, where $k_a = (c_p/c_v)_a$.

The analysis of the nozzle flow from (2) to (a,out) consists of the first law statement and the definition of nozzle isentropic efficiency (Moran and Shapiro, 1995),

$$c_{pa}(T_2 - T_{a,out}) = \frac{1}{2}\left(V_{a,out}^2 - V_2^2\right) \quad (11)$$

$$\eta_n = \frac{c_{pa}(T_2 - T_{a,out})}{c_{pa}(T_2 - T_{3,rev})} \lesssim 1 \quad (12)$$

The state (3,rev) is located on *Figure 1* by intersecting $P_{3,rev} = P_a$ with $s_2 = s_{3,rev}$, namely

$$0 = c_{pa} \ln \frac{T_2}{T_{3,rev}} - R_a \ln \frac{P_2}{P_a} \quad (13)$$

The dimensionless summary of Eqs.(11)-(13) is

$$\tilde{T}_2 - \tilde{T}_{a,out} = \frac{1}{2}\left(v_{a,out}^2 - v_2^2\right) \quad (14)$$

$$\eta_n = \frac{\tilde{T}_2 - \tilde{T}_{a,out}}{\tilde{T}_2 - \tilde{T}_{3,rev}} \quad (15)$$

$$\tilde{T}_2 = \tilde{T}_{3,rev}\, \tilde{P}_2^{b_a} \quad (16)$$

3. Heat Transfer Analysis

The heat exchanger analysis is constructed in terms of effectiveness and number of heat transfer units,

$$\varepsilon = \frac{\tilde{T}_e - \tilde{T}_{e,out}}{\tilde{T}_e - 1} \quad (17)$$

$$\varepsilon = \mu\, \frac{\tilde{T}_{a,out} - 1}{\tilde{T}_e - 1} \quad (18)$$

$$N = \frac{UA}{\dot{m}_e c_{pe}} \quad (19)$$

The combined first law and heat transfer analysis of the heat exchanger yields the function

$$\varepsilon = F\,(N, \mu, \text{configuration}) \quad (20)$$

which is available for several stream-to-stream arrangements in the literature (Bejan, 1993).

The next task is to relate the heat transfer and pressure drop characteristics of the heat exchanger to the properties at states (1) and (2), which appeared in the analyses of the diffuser and the nozzle. The overall thermal resistance $(UA)^{-1}$ is the sum of three resistances, namely convection on the engine air side, conduction through the heat exchanger wall, and convection on the ram air side,

$$\frac{1}{N} = \frac{\dot{m}_e c_{pe}}{UA} = \dot{m}_e c_{pe}\left(\frac{1}{h_c A_c} + \frac{t_w}{k_w A_w} + \frac{1}{h_a A_a}\right) \quad (21)$$

In this equation h_e and h_a are the average heat transfer coefficients based on the contact surfaces A_e and A_a, respectively. The separating wall has the thickness1 t_w and thermal conductivity k_w. The conduction cross-section A_w is an appropriately defined average between A_e and A_a. The heat transfer coefficients are available in the literature in the form of Stanton number correlations

$$\frac{h_e}{c_{pe}G_e} = St_e(Re_e) \quad (22)$$

$$\frac{h_a}{c_{pa}G_a} = St_a(Re_a) \quad (23)$$

where G_e and G_a are the mass velocities based on the flow cross-sectional areas A_{ce} and A_{ca},

$$G_e = \frac{\dot{m}_e}{A_{ce}} \quad G_a = \frac{\dot{m}_a}{A_{ca}} \quad (24)$$

and Re_e and Re_a are the respective Reynolds numbers based on hydraulic diameters

$$Re_e = \frac{G_e D_{he}}{\mu_e} \quad Re_a = \frac{G_a D_{ha}}{\mu_a} \quad (25)$$

Equations (21)-(25) are discussed further in the next section, after assuming a specific geometric arrangement of the two streams. At this stage we can also list the formulas for evaluating the pressure drop along the engine air side

$$\Delta P_e = \frac{G_e^2}{2\rho_e}\left[\left(K_{ce} + 1 - \sigma_e^2\right) + 2\left(\frac{\rho_e}{\rho_{e,out}} - 1\right) + f_e \frac{A_c}{A_{ce}}\frac{\rho_e}{\bar{\rho}_e} - \left(1 - \sigma_e^2 - K_{ee}\right)\frac{\rho_e}{\rho_{e,out}}\right] \quad (26)$$

$$\bar{\rho}_e = \frac{2\rho_e\, \rho_{e,out}}{\rho_e + \rho_{e,out}} \quad (27)$$

and the pressure drop along the ram air side,

$$\Delta P_a = \frac{G_a^2}{2\rho_1}\left[\left(K_{ca} + 1 - \sigma_a^2\right) + 2\left(\frac{\rho_1}{\rho_2} - 1\right) + f_a \frac{A_c}{A_{ca}}\frac{\rho_1}{\bar{\rho}_a} - \left(1 - \sigma_a^2 - K_{ea}\right)\frac{\rho_1}{\rho_2}\right] \quad (28)$$

$$\bar{\rho}_a = \frac{2\rho_1\rho_2}{\rho_1 + \rho_2} \tag{29}$$

The contraction and enlargement loss coefficients (K_c, K_e) for various geometries are available in the literature (Kays and London, 1984). The flow cross-section reduction factors are

$$\sigma_e = \frac{A_{ce}}{A_{fe}} \qquad \sigma_a = \frac{A_{ca}}{A_{fa}} \tag{30}$$

where A_{fe} and A_{fa} are the frontal areas faced by the approaching streams. The friction factors are available as functions of the respective Reynolds numbers,

$$f_e = f_e(Re_e) \qquad f_a = f_a(Re_a) \tag{31}$$

4. Heat Exchanger Geometry

The minimization of the entropy generation rate will be achieved by making appropriate changes in the physical parameters of the system. Most of these parameters account for the dimensions of the flow passages that make up the heat exchanger. In order to determine which of these parameters play trade-off roles that lead to the minimization of N_S, we make the important assumption that every single geometric parameter is not specified in priori. In other words, we depart from the traditional approach in which some geometric features of the heat exchanger are fixed by the "surface type" that may be available in a handbook and on the market. We can return to the commercial surface types only after we have determined the passage dimensions that guarantee operation in the close vicinity of the thermodynamic optimum.

This first phase of our work is aided by the preliminary simplifying assumption that fins are absent. Each channel is a narrow space between two parallel plates of area $L_e \times L_a$, as shown in *Figure 2*. There are n channels in total, n/2 for the $\dot{m}_e$ stream, and n/2 for the $\dot{m}_a$ stream. The channel spacings are D_e and D_a. The height of the heat exchanger is H. The plate thickness t_w is assumed given, as in Eq.(21). There are five dimensions that may vary: L_e, L_a, D_e, D_a and H. The total volume B is an important constraint,

$$B = L_e L_a H \tag{32}$$

which reduces to four the number of geometric degrees of freedom. The cross-flow configuration is also characterized by the relations

$$n = \frac{H}{t_w + (D_e + D_a)/2} \tag{33a}$$

$$A_e = A_w = A_a = n L_e L_a \tag{33b}$$

$$\sigma_e = \frac{D_e}{2t_w + D_e + D_a} \tag{34a}$$

$$\sigma_a = \frac{D_a}{2t_w + D_e + D_a} \tag{34b}$$

$$\frac{A_{ce}}{A_e} = \frac{1}{2}\frac{D_e}{L_e} \qquad \frac{A_{ca}}{A_a} = \frac{1}{2}\frac{D_a}{L_a} \tag{35}$$

$$m = \rho_w t_w n L_e L_a \tag{36}$$

where m is the total mass of the heat exchanger.

We place the entire thermodynamic optimization procedure on a fixed-volume basis [more on this when we discuss Eq.(41)] by using $B^{1/3}$ as length scale in the nondimensionalization of all the lengths:

$$\left(\tilde{L}_e, \tilde{L}_a, \tilde{D}_e, \tilde{D}_a, \tilde{H}\right) = (L_e, L_a, D_e, D_a, H)/B^{1/3} \tag{37}$$

The heat transfer and pressure drop relations (21), (26) and (28) assume, in order, the following dimensionless forms

$$\frac{1}{N} = \frac{1}{2St_e}\frac{D_e}{L_e} + \frac{\dot{m}_e c_{pe} t_w}{k_w B^{2/3}} \frac{1}{n\tilde{L}_e\tilde{L}_a} + \frac{1}{\mu}\frac{1}{2St_a}\frac{D_a}{L_a} \tag{38}$$

$$\tilde{P}_e - \tilde{P}_{e,out} = \frac{\dot{m}_e^2}{\rho_e P_a B^{4/3}} \frac{2}{\left(n\tilde{D}_e\tilde{L}_a\right)^2}$$

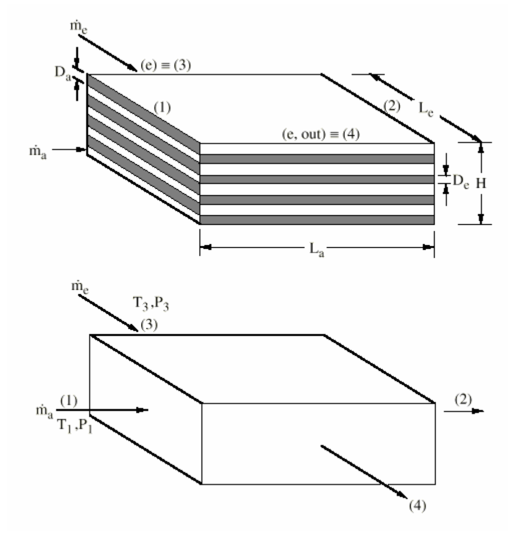

Figure 2. Cross-flow arrangement consisting of parallel-plate channels.

$$\left[\left(K_{ce} + 1 - \sigma_e^2 \right) + 2\left(\frac{\rho_e}{\rho_{e,out}} - 1 \right) + 2 f_e \frac{L_e}{D_e} \frac{\rho_e}{\bar{\rho}_e} - \left(1 - \sigma_e^2 - K_{ee} \right) \frac{\rho_e}{\rho_{e,out}} \right] \tag{39}$$

$$\tilde{P}_1 - \tilde{P}_2 = \frac{\dot{m}_a^2}{\rho_1 P_a B^{4/3}} \frac{2}{\left(n\tilde{D}_a \tilde{L}_e \right)^2} \left[\left(K_{ca} + 1 - \sigma_a^2 \right) + 2 f_a \frac{L_a}{D_a} \frac{\rho_1}{\bar{\rho}_a} - \left(1 - \sigma_a^2 - K_{ea} \right) \frac{\rho_1}{\rho_2} \right] \tag{40}$$

Equations (38)-(40) reveal the ratio $\dot{m}_e / B^{2/3}$, in which both $\dot{m}_e$ and B are specified. We account for this ratio by defining the dimensionless number

$$R = \frac{\dot{m}_e}{B^{2/3} (\rho_e P_a)^{1/2}} \tag{41}$$

The factors that contain B in Eqs.(38)-(40) become

$$\frac{\dot{m}_e c_{pe} t_w}{k_w B^{2/3}} = R \frac{t_w}{k_w} c_{pe} \rho_e^{1/2} P_a^{1/2} \tag{42}$$

$$\frac{\dot{m}_e^2}{\rho_e P_a B^{4/3}} = R^2 \tag{43}$$

$$\frac{\dot{m}_a^2}{\rho_1 P_a B^{4/3}} = R^2 \mu^2 \frac{\rho_e}{\rho_1} \left(\frac{c_{pe}}{c_{pa}} \right)^2 \tag{44}$$

The advantage of this formulation is that it begins to show analytically that certain geometric features play trade-off roles in the thermodynamic design. For example, Eqs.(38) and (39) show that the channel slenderness ratio D_e/L_e can be varied to trade "improved heat transfer" for "decreased friction", and vice versa. The same role is played by D_a/L_a, as shown by Eqs.(38) and (40).

5. The Generation of Entropy in the Heat Exchanger

We start with the innermost part of the system—the crossflow heat exchanger—and optimize its geometry subject to its volume and mass constraints, Eqs.(32) and (36). We assume temporarily that the heat exchanger is isolated from the rest of the system of *Figure 1*, as shown in the lower part of *Figure 2*. The two streams $(\dot{m}_a, \dot{m}_e)$ are specified, and so are the two inlet states, (T_1, P_1) and (T_3, P_3). The outlet conditions (T_2, P_2) and (T_4, P_4) are the four unknowns that will be determined from the heat transfer and pressure drop analysis of the core. For consistency, we changed the names of states (e) and (e, out) to (3) and (4), respectively.

The heat transfer Eqs.(17)-(18) become

$$\varepsilon = \frac{\tilde{T}_3 - \tilde{T}_4}{\tilde{T}_3 - \tilde{T}_1} \tag{45}$$

$$\varepsilon = \mu \frac{\tilde{T}_2 - \tilde{T}_1}{\tilde{T}_3 - \tilde{T}_1} \tag{46}$$

and, in conjunction with Eq.(20) they deliver $\tilde{T}_4$ and $\tilde{T}_2$. The overall number of heat transfer units relation (38) can now be rewritten as

$$\frac{1}{N} = \frac{1}{2St_e} \frac{D_e}{L_e} + R\hat{t}_w \frac{1}{n\tilde{L}_e \tilde{L}_a} + \frac{1}{\mu} \frac{1}{2St_a} \frac{D_a}{L_a} \tag{47}$$

where the dimensionless wall thickness

$$\hat{t}_w = t_w c_{pe} \rho_e^{1/2} P_a^{1/2} / k_w \tag{48}$$

should not be confused with $\tilde{t}_w = t_w/B^{1/3}$. The pressure-drop Eqs.(39-40) become

$$\tilde{P}_3 - \tilde{P}_4 = \frac{2R^2}{\left(n\tilde{D}_e \tilde{L}_a \right)^2} \left[\left(K_{ce} + 1 - \sigma_e^2 \right) + 2\left(\frac{\rho_3}{\rho_4} - 1 \right) \right.$$

$$(49)$$

$$\tilde{P}_1 - \tilde{P}_2 = \frac{\rho_3 c_{pe}^2}{\rho_1 c_{pa}^2} \frac{2\mu^2 R^2}{\left(n\tilde{D}_a \tilde{L}_e \right)^2} \left[\left(K_{ca} + 1 - \sigma_a^2 \right) + 2\left(\frac{\rho_1}{\rho_2} - 1 \right) + 2 f_a \frac{L_a}{D_a} \frac{\rho_1}{\bar{\rho}_a} - \left(1 - \sigma_a^2 - K_{ea} \right) \frac{\rho_1}{\rho_2} \right] \tag{50}$$

while the average density definitions (27) and (29) continue to apply. Invoking the ideal gas model for each stream, we can also write

$$\frac{\rho_3}{\rho_4} = \frac{\tilde{P}_3 \tilde{T}_4}{\tilde{P}_4 \tilde{T}_3} \qquad \frac{\rho_1}{\rho_2} = \frac{\tilde{P}_1 \tilde{T}_2}{\tilde{P}_2 \tilde{T}_1} \tag{51}$$

The four outlet properties $\left(\tilde{T}_2, \tilde{P}_2, \tilde{T}_4, \tilde{P}_4 \right)$ calculated based on Eqs.(45-46) and (49, 50) are finally substituted into the entropy generation number of the heat exchanger, N_S^{he}, which has to be minimized:

$$N_S^{he} = \ln \frac{\tilde{T}_4}{\tilde{T}_3} - b_e \ln \frac{\tilde{P}_4}{\tilde{P}_3} + \mu \left(\ln \frac{\tilde{T}_2}{\tilde{T}_1} - b_a \ln \frac{\tilde{P}_2}{\tilde{P}_1} \right) \tag{52}$$

Equations (45)-(50) show that the N_S^{he} calculation also depends on the geometry of the heat exchanger, which is characterized by 8 variables: $\tilde{L}_a, \tilde{D}_a, \tilde{L}_e$, $\tilde{D}_e, \tilde{H}, n, \sigma_a$ and σ_e. The wall thicknessÿÿ EMBED "Eq36ÿÿ " * mergeformat $\hat{t}_w \left(\text{or } \tilde{t}_w \right)$ is assum h kt wnÿÿ The 8 variables are related through equations (33a) and

(34),

$$n = \frac{\tilde{H}}{\tilde{t}_w + \left(\tilde{D}_e + \tilde{D}_a\right)/2} \quad (53)$$

$$\sigma_e = \frac{\tilde{D}_e}{2\tilde{t}_w + \tilde{D}_e + \tilde{D}_a} \qquad \sigma_a = \frac{\tilde{D}_a}{2\tilde{t}_w + \tilde{D}_e + \tilde{D}_a} \quad (54)$$

and the volume and mass constraints (32) and (36),

$$\tilde{L}_e \tilde{L}_a \tilde{H} = 1 \quad (55)$$

$$\tilde{t}_w \, n \, \tilde{L}_e \tilde{L}_a = \phi \quad (56)$$

The dimensionless parameter ϕ accounts for the total mass of the core,

$$\phi = m/(\rho_w B) \quad (57)$$

and can be interpreted as a volume fraction: the fraction occupied by all the solid walls in the entire volume B. In view of the 5 geometric relations (53) - (56), there are only three degrees of freedom in the core geometry, for example,

$$N_S^{he} = \text{function}\left(\frac{D_e}{D_a}, \tilde{L}_a, \tilde{H}\right) \quad (58)$$

The final ingredient in this analytical model is the characterization of the heat transfer surface. For simplicity, we assume fully developed flow between parallel plates, such that for each duct we may use the laminar and turbulent flow correlations (Bejan, 1993):

$$f = \frac{24}{Re_{D_h}} \qquad St = \frac{8.235}{Re_{D_h} Pr} \quad (Re_{D_h} < 2300) \quad (59)$$

$$f = 0.078\, Re_{D_h}^{-1/4} \quad \left(2300 < Re_{D_h} < 8\times10^4\right) \quad (60a)$$

$$f = 0.046\, Re_{D_h}^{-1/5} \quad \left(2\times10^4 < Re_{D_h} < 10^6\right) \quad (60b)$$

$$St = \frac{f}{2} Pr^{-2/3} \quad (60c)$$

We also used the simpler Reynolds number notation Re_{D_h} + Re, so that for the duct of spacing D_e we write $D_{h,e} = 2D_e$ and

$$Re_e = \frac{\dot{m}_e/(n/2)}{D_e L_a} \cdot \frac{2D_e}{\mu_e} = \frac{4}{n} \frac{}{\tilde{L}_a} R\tilde{B} \quad (61)$$

and similarly

$$Re_a = \frac{\dot{m}/(n/2)}{D_a L_e} \cdot \frac{2D_a}{\mu_a} = \frac{4}{n\tilde{L}_e} RB\mu \frac{\mu_e c_{pe}}{\mu_a c_{pa}} \quad (62)$$

where $\tilde{B}$ is a dimensionless version of the specified size (length scale $B^{1/3}$) of the heat exchanger core,

$$\tilde{B} = B^{1/3} \left(\rho_e P_a\right)^{1/2} / \mu_e \quad (63)$$

The $\tilde{B}$ dimension is assumed known, for example $\tilde{B} = 10^7$, which corresponds physically to the volume scale $B = 0.5m^3$ (TABLE I). This dimension also dictates the proportionality between $\hat{t}_w$ and $\hat{t}_w$,

$$\hat{t}_w = \tilde{t}_w \; \tilde{B} \, Pr_e \frac{k_e}{k_w} \quad (64)$$

and the way to calculate the R parameter (41),

$$R = \tilde{m} / \tilde{B}^2 \quad (65)$$

where $\tilde{m}$ is the specified dimensionless mass flow rate on the engine-air side,

$$\tilde{m} = \dot{m}_e \left(\rho_e P_a\right)^{1/2} / \mu_e^2 \quad (66)$$

In summary, the friction factors and Stanton numbers appearing in Eqs.(47) and (49-50) are calculated after the Reynolds numbers (61, 62), by using Eqs.(59)-(60).

6. Optimization of the Heat Exchanger Geometry

The numerical work consisted of minimizing the heat exchanger entropy generation rate N_S^{he}, Eqs.(52) and (58), by varying three geometric features of the core architecture. This optimization work is illustrated sequentially in *Figures 3-7*. The calculations were performed for the reference case defined by the physical and dimensionless parameters shown in TABLE I.

The first optimization opportunity is presented by the ratio D_e/D_a, because we can expect large pressure drop irreversibilities in both extremes, $D_e \ll D_a$ and $D_e \gg D_a$. This behavior is confirmed by *Figure 3*, which shows the effect of D_e/D_a on the heat exchanger irreversibility N_S^{he}, when the other two geometric parameters $\left(\tilde{L}_a, \tilde{H}\right)$ are fixed. The figure also shows how this irreversibility is divided between the heat transfer and fluid friction effects. The lower curve $\left(N_{S,\Delta T}^{he}\right)$ represents the irreversibility due solely to heat transfer across finite temperature differences: this portion was calculated based on the two temperature-ratio terms that appear in Eq.(52). The difference between the two ordinate values $\left(N_S^{he} - N_{S,\Delta T}^{he}\right)$ represents the pressure drop irreversibility, or the two pressure-ratio terms that are present in Eq.(52).

TABLE I. Physical and dimensionless parameters for the heat exchangers optimized in *Figures 3-7*.

$B = 0.5\ m^3$	$R = \tilde{m} / \tilde{B}^2 = 10^{-3}$
$\tilde{B} = 10^7$	$R_a = R_e = 0.287$ kJ $kg^{-1}\ K^{-1}$
$c_{pa} = c_{pe} = 1$ kJ $kg^{-1}\ K^{-1}$	$t_w = 0.4$ mm
$k_a = 0.02\ W\ m^{-1}\ K^{-1}$	$\tilde{t}_w = 5 \infty 10^{-4}$
$k_e = 0.03\ W\ m^{-1}\ K^{-1}$	$\hat{t}_w = 0.512$
$k_w = 205\ W\ m^{-1}\ K^{-1}$	$T_a = 245$ K
$\dot{m}_a = 0.84\ kg\ s^{-1}$	$T_1 = 245$ K
$\dot{m}_e = 0.16\ kg\ s^{-1}$	$\tilde{T}_1 = 1$
$\tilde{m} = 10^{11}$	$T_3 = 360$ K
$P_a = P_1 = 31$ kPa	$\tilde{T}_3 = 1.47$
$\tilde{P}_1 = 1$	$\mu = 5.33$
$P_3 = 269$ k Pa	$\mu_a = 1.55 \infty 10^{-5}$ W $s^{-1}\ m^{-1}$
$\tilde{P}_3 = 8.7$	$\mu_e = 2.12 \infty 10^{-5}$ W $s^{-1}\ m^{-1}$
$Pr_a = Pr_e = 0.7$	$\phi = 0.1$

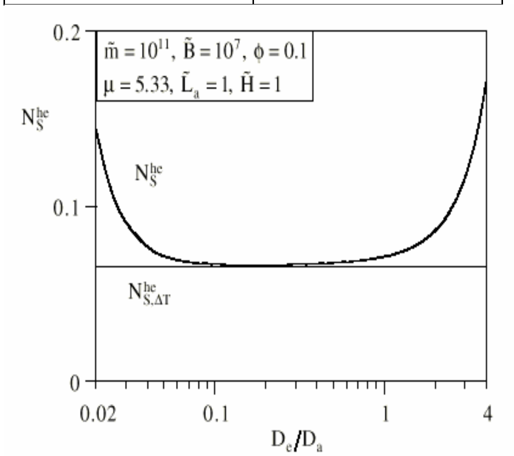

Figure 3. The first minimization of the heat exchanger entropy generation rate.

It is clear that the heat exchanger irreversibility has a minimum with respect to D_e/D_a, and that this minimum is due almost entirely to the variation of the pressure drop irreversibility. The heat transfer irreversibility is relatively insensitive to changes in D_e/D_a. At the optimum the entropy generation rate is dominated by the irreversibility due to heat transfer.

We search for a second minimization of the heat exchanger irreversibility by varying the dimension $\tilde{L}_a$ while continuing to hold $\tilde{H}$ fixed. Since the volume $\tilde{L}_a\ \tilde{L}_e\ \tilde{H}$ is constrained, this optimization is the same as selecting the shape (aspect ratio L_a/L_e) of each rectangular heat transfer surface, or trading off the flow length of one stream for the flow length of the other.

This procedure is illustrated in *Figure 4*. Plotted on the ordinate is the entropy generation rate already minimized with respect to D_e/D_a: this number is labeled $N_{S,m}^{he}$, where the subscript "m" stands for "minimized once". *Figure 4* was constructed by repeating for many $\tilde{L}_a$ cases the procedure of *Figure 3*. In this way we find that the entropy generation rate has a minimum with respect to $\tilde{L}_a$. At this minimum the entropy generation rate is dominated by heat transfer effects $\left(N_{S,m,\Delta T}^{he}\right)$, and the contribution due to the pressure drops $\left(N_{S,m}^{he} - N_{S,m,\Delta T}^{he}\right)$ is minor.

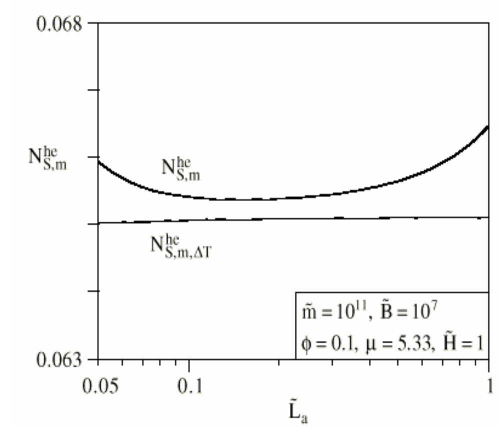

Figure 4. The variation of the minimized entropy generation rate with respect to the flow length $\tilde{L}_a$.

The resulting figure of merit of the second minimization is the entropy generation number $N_{S,mm}^{he}$ plotted in *Figure 5*. On the abscissa varies the third geometric feature of the heat exchanger, $\tilde{H}$. *Figure 5* was generated by repeating many times the nested optimization loops illustrated in *Figures 3* and *4*. The conclusion is that a third minimization is not possible, i.e., an optimal dimension $\tilde{H}$ does not exist.

The top frame of *Figure 6* reports the optimal ratio of channel spacings, and shows that $(D_e/D_a)_{opt}$ is of order 1 and relatively insensitive to the assumed $\tilde{H}$ value. The same figure shows the corresponding number of channels: n increases with the transversal dimension $\tilde{H}$.

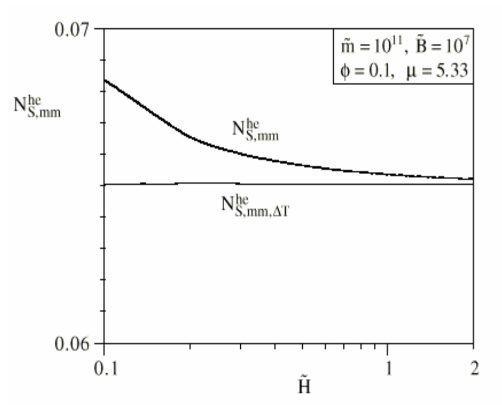

Figure 5. The heat exchanger entropy generation rate minimized with respect to D_e/D_a and $\tilde{L}_a$, and its variation versus the third geometric parameter of the heat exchanger ($\tilde{H}$).

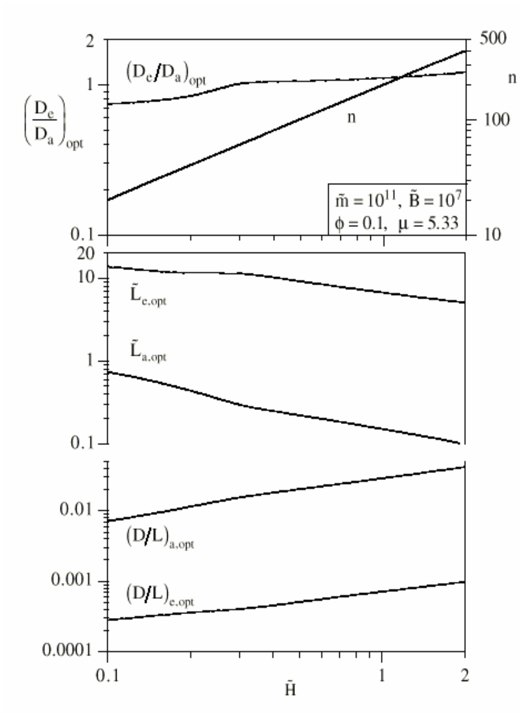

Figure 6. The ratio of channel spacings, number of channels and channel aspect ratios that correspond to the system optimized in Fig. 5.

The streamwise dimensions of the twice-optimized heat exchangers are reported in the middle part of *Figure 6*. The lengths $\tilde{L}_{e,opt}$ and $\tilde{L}_{a,opt}$ differ by a factor of order 10, and decrease gradually as the transversal dimension $\tilde{H}$ increases. The lower part of the figure reports the corresponding slenderness ratios of the flow channels, $(D/L)_e$ and $(D/L)_a$. These ratios are sufficiently small, so that the fully developed laminar or turbulent flow assumption [Eqs.(59)-(60)] is justified. In the range $0.1 < \tilde{H} < 2$ covered by *Figures 5* and *6* the channel Reynolds numbers (Re_a, Re_e) vary in the range 200-2300.

In the same $Re_{a,e}$ range the effectiveness is greater than 0.99, and the number of heat transfer units is greater than 10. Both ε and N are practically insensitive to changes in $\tilde{H}$.

As an alternative to the local minimization of $N_{S,m}^{he}$ (*Figure 4*), we fixed from the outset $\tilde{L}_a = 1$ and proceeded with the optimization with respect to D_e/D_a. The optimized spacings and channel aspect ratios are presented in *Figure 7*. These results can be compared directly with *Figure 6* to see that the optimization of $\tilde{L}_a$ has a significant effect on the spacings ratio $(D_e/D_a)_{opt}$, no effect on the number of channels, and only a weak effect on the slenderness ratios of the two channel shapes.

The geometric optimization results are sensitive to changes in other parameters that until now were fixed. The effect of changing the capacity rate ratio μ is documented in *Figure 8*.

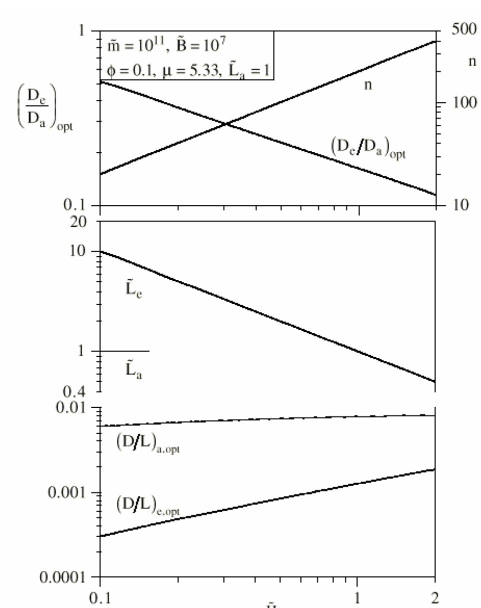

Figure 7. Optimal ratio of channel spacings and number of channels when $\tilde{L}_a = 1$, and the corresponding streamwise dimensions and channel aspect ratios.

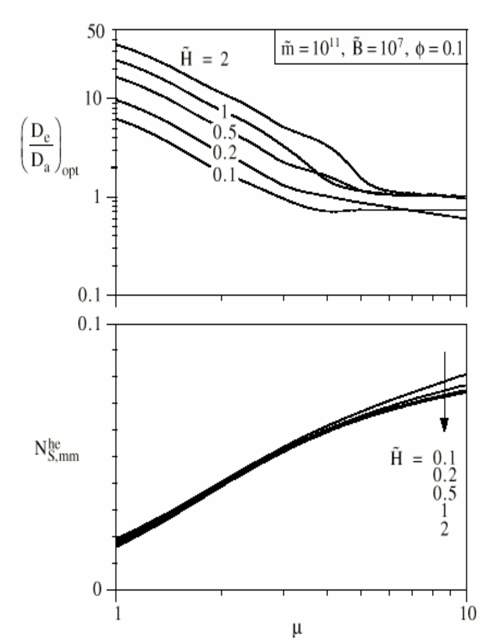

Figure 8. The effect of the capacity rate ratio on the ratio of channel spacings, and on the minimized entropy generation rate.

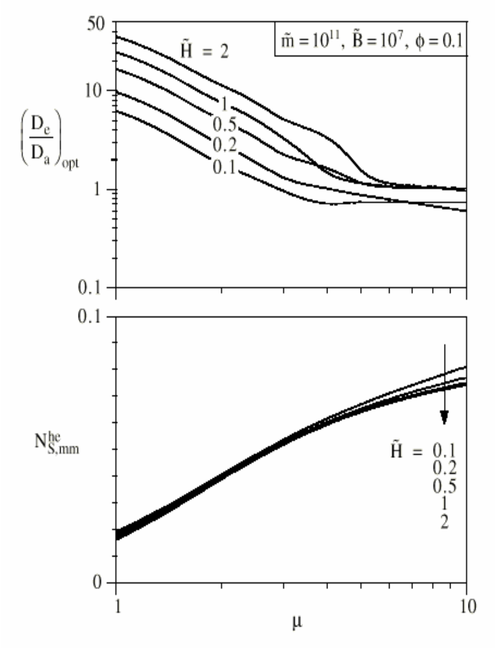

Figure 8. The effect of the capacity rate ratio on the ratio of channel spacings, and on the minimized entropy generation rate.

The results were generated by repeating for several μ values the double optimization procedure that led to *Figure 6*. The upper graph in *Figure 8* shows that the capacity rate ratio has an effect on the order of magnitude of $(D_e/D_a)_{opt}$ when μ is smaller than approximately 5, above this μ value the ratio $(D_e/D_a)_{opt}$ is approximately equal to 1, i.e., insensitive to changes in μ and $\tilde{H}$. The lower graph shows the corresponding entropy generation number, which increases with μ and is practically insensitive to changes in $\tilde{H}$. Not shown in *Figure 8* are the corresponding aspect ratios of the two channels, $(D_a/L_a)_{opt}$ and

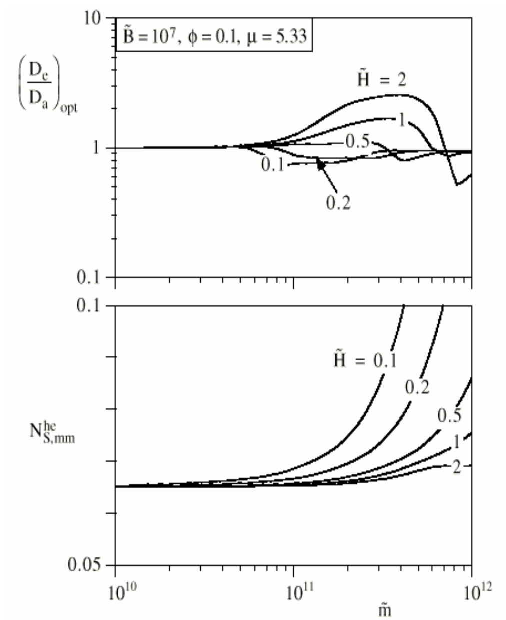

Figure 9. The effect of the engine-air mass flow rate on the channel spacings ratio and the corresponding entropy generation rate.

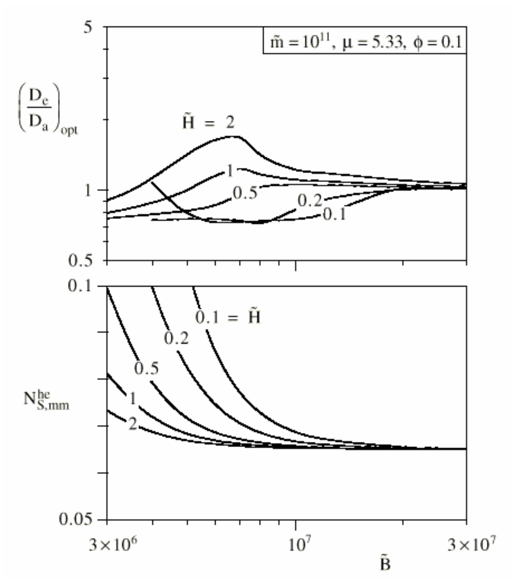

Figure 10. The effect of the heat exchanger core volume on the channel spacings ratio and the corresponding entropy generation rate.

$(D_e/L_e)_{opt}$, which are consistently of order 10^{-2} and 10^{-3}, respectively. The numerical results also show that the capacity rate ratio has no effect on the required number of channels, n: these results are also omitted.

The mass flow rate on the engine-air side is represented by the dimensionless group $\tilde{m}$. The effect of changes in this parameter is documented in *Figure 9*. The spacings ratio $(D_e/D_a)_{opt}$ is consistently of order 1. The lower part of *Figure 9* shows that the entropy generation rate is practically constant when $\tilde{m}$ is smaller than the reference value of 10^{11}, and that $\tilde{H}$ has a noticeable effect when $\tilde{m}$ is greater than 10^{11}. The same series of numerical results show that $\tilde{m}$ has no effect on the number of channels that corresponds to each of these designs. Throughout the range covered by *Figure 9* the orders of magnitude of $(D_a/L_a)_{opt}$ and $(D_e/L_e)_{opt}$ are 10^{-2} and 10^{-3} respectively.

The volume of the heat exchanger core ($\tilde{B}$) does not affect the order of magnitude of $(D_e/D_a)_{opt}$ as $\tilde{B}$ and $\tilde{H}$ increase. This effect is shown in the upper part of *Figure 10*. The corresponding number of channels (n) is insensitive to $\tilde{B}$ in the range investigated. In the same range the channel aspect ratios $(D_a/L_a)_{opt}$ and $(D_e/L_e)_{opt}$ maintain their orders of magnitude, 10^{-2} and 10^{-3}, respectively. The lower frame of *Figure 10* shows that the volume has an effect on the entropy generation rate when $\tilde{B}$ and $\tilde{H}$ decrease.

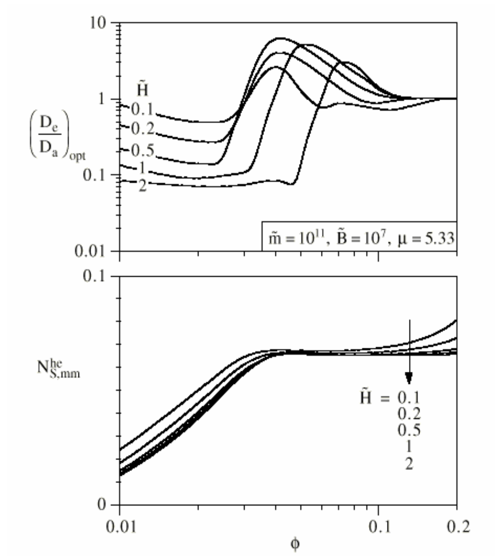

Figure 11. The effect of the volume fraction occupied by the solid parts of the heat exchanger core.

The volume fraction occupied by all the solid parts of the core (ϕ) has a noticeable effect on the spacings ratio as ϕ decreases: see the upper frame of *Figure 11*. In the same limit the calculated aspect ratios of the two channels become insensitive to decreases in ϕ, namely $(D_a/L_a)_{opt} \sim 10^{-2}$ and $(D_e/L_e)_{opt} \sim 10^{-3}$. The corres-ponding number of channels (n, not shown) decreases almost proportionally with ϕ and $\tilde{H}$. The lower frame of *Figure 11* reports the corresponding entropy generation number, which decreases weakly and monotonically with ϕ.

7. Minimization of the Total Entropy Generation Rate

We now reconsider the entire optimization procedure by focusing on the total entropy generation rate, Eqs.(1) and (4). Instead of accounting only for the irreversibility of the heat exchanger (sections 5 and 6), we now include the entropy generated by the diffuser, nozzle and mixing undergone by the exhaust.

In this new analysis the streams $(\dot{m}_a, \dot{m}_e)$ are specified, and so are the inlet states of the diffuser (T_a, P_a) and engine air (T_3, P_3). The diffuser and nozzle efficiencies are specified, $\eta_d = 0.97$ and $\eta_n = 0.95$. The diffuser inlet state is also specified: T_a, P_a and $M_a = 0.34$, which coresponds to $V_a = 107$ m/s. The heat transfer and pressure drop analyses of the diffuser, heat exchanger and nozzle (sections 2-4) allow us to determine the four unknowns of the problem: the outlet temperature and velocity of the nozzle ($T_{a,out}$, $V_{a,out}$) and the outlet conditions of the heat exchanger (T_4, P_4). With these values known, the entropy generation number is finally calculated from Eq.(4).

As in the optimization of the isolated heat exchanger, we regard N_S as a function of three dimensionless parameters, D_e/D_a, $\tilde{L}_a$ and $\tilde{H}$. In the first phase of the numerical work we minimized the total entropy generation rate with respect to D_e/D_a while holding $\tilde{L}_a$ and $\tilde{H}$ fixed. The results obtained en route to $N_{S,m}$ and $(D_e/D_a)_{opt}$ are qualitatively similar to what we saw in *Figure 3*, and are not shown.

The second phase of the numerical work focused on the second minimum: the minimization of $N_{S,m}$ with respect to $\tilde{L}_a$. The resulting $N_{S,m}$ curve has the same behavior versus $\tilde{H}$ as the $N^{he}_{S,mm}$ curve of *Figure 5*. The $N_{S,mm}$ value, however, is almost three times greater than $N^{he}_{S,mm}$ because of the additional irreversibility contributions made by the diffuser, nozzle and mixing with the ambient.

The resulting geometric characteristics of the optimized design are reported in *Figure 12*. These should be compared with the corresponding quantities obtained by minimizing the heat exchanger irreversibility alone, *Figure 6*. The ratio of channel spacings (*Figure 12*) is larger by a factor of ten or more than in *Figure 6*: the performance of the greater system is optimized when the engine-air passages are ten or more times wider than the ram-air passages. The lower portion of the $(D_e/D_a)_{opt}$ curve in *Figure 12* is a reflection of the Reynolds number on the engine-air side, which passes through the laminar-turbulent transition as $\tilde{H}$ decreases (Re_e = 2300). In the same range the ram-air flow through the heat exchanger persists in the laminar regime.

The upper graph in *Figure 12* also shows that the required number of channels (n) is practically the same as when the heat exchanger irreversibility was minimized alone (*Figure 6*). The channel lengths and slenderness ratios shown in the lower part of *Figure 12* have the same order of magnitude and behavior as in the preceding sections (*Figure 6*). The same can be said about the heat exchanger effectiveness and number of heat transfer units, which are comparable with the earlier results, $\varepsilon \gtrsim 0.99$ and $N \gtrsim 12$. This degree of robustness is remarkable, especially if we consider the occurrence of the laminar-turbulent transition on the engine-air side, in the case of *Figure 12*.

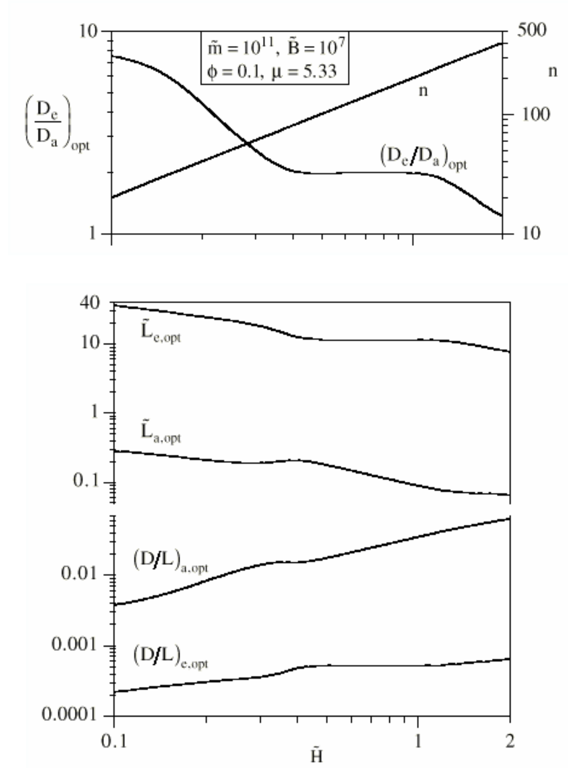

Figure 12. The ratio of channel spacings, number of channels and slenderness ratios that correspond to the double minimization of the total rate of entropy generation.

The thermodynamic optimization of the complete system of *Figure 1* continued with the numerical study of the individual effects of μ, $\tilde{m}$, $\tilde{B}$ and ϕ on the twice-minimized entropy generation rate and the associated geometric features. The behavior of these results is not shown because it parallels what we saw earlier in *Figures 8-11*. New effects that deserve to be investigated at the complete-system level are the approach velocity V_a and the diffuser and nozzle efficiencies.

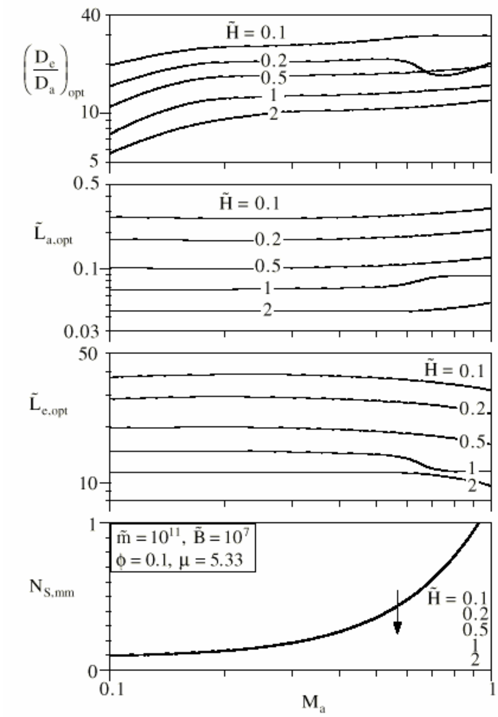

Figure 13. The effect of the approach Mach number on the optimized internal geometry of the heat exchanger.

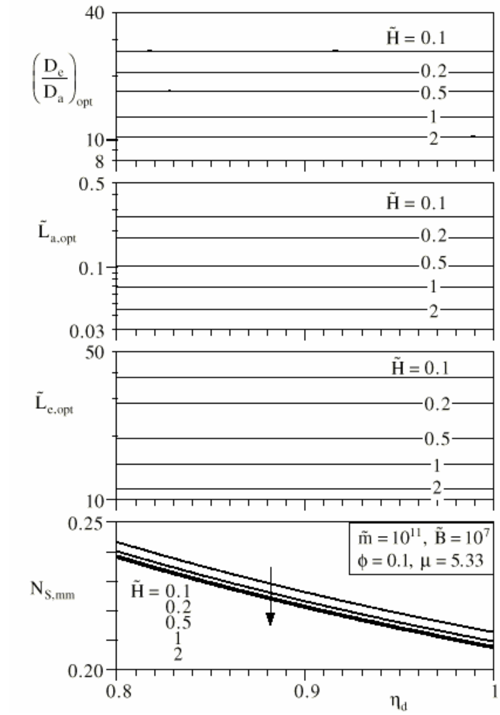

Figure 14. The effect of the diffuser efficiency on the optimized internal geometry of the heat exchanger.

Figure 13 shows the effect of the air stream relative velocity, which is represented by the Mach number M_a on the abscissa. The effect on the optimized geometric parameters D_e/D_a, $\tilde{L}_e$ and $\tilde{L}_a$ is weak, regardless of the relative height of the heat exchanger core ($0.1 < \tilde{H} \leq 2$). The optimized internal structure of the heat exchanger is robust with respect to changes in the external (global) parameter M_a. The bottom graph of *Figure 13* confirms a trend that was expected: the minimized entropy generation rate increases monotonically as the relative velocity increases.

More robustness is documented in *Figure 14,* which shows the effect of varying the diffuser efficiency in the range $0.8 \leq \eta_d \leq 1$. The effect on the optimized geometric features of the heat exchanger core is imperceptible. As expected, the total entropy generation rate decreases monotonically as η_d increases. The diffuser irreversibility is not negligible, because $N_{S,mm}$ decreases by more than 10 percent as η_d increases from 0.8 to 1.

It can be shown analytically that the nozzle efficiency has no effect on the total entropy generation rate, Eq.(4), and, consequently, no effect on the optimized geometry of the heat exchanger. The reason is that the entropy generation rate due to thermal and mechanical mixing with the ambient, from state (a,out) to (0), is included in the total entropy generation rate (1). The exergy savings that would be registered in the nozzle section by increasing η_n are destroyed immediately downstream of the nozzle.

8. Conclusion

The main conclusion of this study is that it is possible to determine several of the main architectural features of a relatively complicated system by optimizing it thermodynamically subject to global constraints. The crossflow heat exchanger with ram air flow on the cold side (*Figure 1*) was used as an example. The optimized geometric features were robust relative to changes in other physical parameters, such as the core height $\tilde{H}$ in *Figure 6*, or the solid fraction ϕ in *Figure 11*.

More robustness emerged when we included in the entropy generation formula the contribution made by the discharging of the air stream [state (a,out)] into the ambient [state (0)]. The optimized geometric features are relatively insensitive to this additional and thermodynamically relevant irreversibility. The reason, we think, is that the heat exchanger cases optimized in the first part of the study had relatively high ε and N values. In this range the minimization of the heat exchanger irreversibility in isolation "makes sense", as explained in the maximum-$\dot{S}_{gen}$ paradox discussed in Bejan (1997), pp. 604-609. In other words, in this (ε, N) range the principle of proper thermodynamic isolation is satisfied and, as a preliminary step, the heat exchanger can be optimized alone.

The system analyzed and optimized in this study showed that opportunities for geometric optimization can be identified based on relatively simple but realistic models subjected to constraints that are ultimately related to economic considerations. Once identified, these optimization opportunities deserve to be pursued in engineering practice, based on considerably more refined models with more systems parameters. The robustness of the optimum relative to certain parameters may be used to simplify future optimizations of similar combined systems.

Acknowledgment

The authors acknowledge with gratitude the guidance provided in this research project by Mr. David L. Siems of the Boeing Corporation. This material is based upon work supported by the Air Force Office of Scientific Research under Contract No. F49620-98-C-0007. Any opinions, findings and conclusions or recommendations are those of the authors and do not necessarily reflect the views of the Air Force Office of Scientific Research. Asad Alebrahim acknowledges with gratitude the support received from Kuwait University.

Nomenclature

A	heat transfer area, m^2
A_c	cross-sectional area, m^2
A_f	frontal area, m^2
b	dimensionless constant, R/c_p
B	volume, m^3
c_p	specific heat at constant pressure, J kg^{-1} K^{-1}
C	capacity rate, WK^{-1}
D	spacing, m
D_h	hydraulic diameter, m
f	friction factor
G	mass velocity, kg m^{-2} s^{-1}
h	heat transfer coefficient, W m^{-2} K^{-1}
H	height, m
k	thermal conductivity, W m^{-1} K^{-1}
k_a	c_p/c_v of air
$K_{c,e}$	contraction and expansion coefficients
$L_{a,e}$	lengths, m
m	mass, kg
$\dot{m}$	mass flow rate, kg s^{-1}
$\tilde{m}$	dimensionless engine-air flow rate,Eq.(66)
M	Mach number, Eq.(10)
n	number of channels
N	number of heat transfer units, Eq.(19)
N_S	entropy generation number, Eq.(4)
P	pressure, Pa
Pr	Prandtl number
$\dot{Q}_0$	heat transfer rate, W
R	dimensionless factor, Eq.(41)
$R_{a,e}$	ideal gas constants, J kg^{-1} K^{-1}
Re	Reynolds number, Eqs.(25)
s	specific entropy, J kg^{-1} K^{-1}
$\dot{S}_{gen}$	entropy generation rate, W K^{-1}
St	Stanton number
t	thickness, m
$\hat{t}_w$	dimensionless wall thickness, Eq.(48)
T	temperature, K
U	overall heat transfer coefficient, W m^{-2} K^{-1}
V	velocity, m s^{-1}

Greek symbols

ΔP	pressure drop, Pa
ΔT	temperature difference, K
ε	effectiveness, Eqs.(17-18)
η_d	diffuser efficiency
η_n	nozzle efficiency
μ	ratio of capacity rates, Eq.(2)
$\mu_{a,e}$	viscosities, kg s^{-1} m^{-1}
ρ	density, kg m^{-3}
σ	cross-section reduction factor
ϕ	volume fraction occupied by solid walls

Superscripts

he	heat exchanger
~	dimensionless notation, Eqs.(3), (37) and (63)

Subscripts

a	ambient air
e	engine air
m	minimized once
max	maximum
min	minimum
mm	minimized twice

opt	optimum
out	outlet
rev	reversible
w	wall

References

Ahern, J. E., 1980, *The Exergy Method of Energy Systems Analysis*, Wiley, New York.

Bejan, A., 1982, *Entropy Generation through Heat and Fluid Flow*, Wiley, New York.

Bejan, A., 1993, *Heat Transfer*, Wiley, New York.

Bejan, A., 1996, *Entropy Generation Minimization*, CRC Press, Boca Raton.

Bejan, A., 1997, *Advanced Engineering Thermodynamics*, second edition, Wiley, New York.

Bejan, A., 1999, A role for exergy analysis and optimization in aircraft energy-system design, *Proceedings of the ASME Advanced Energy Systems Division*, Aceves, S., ed., ASME, New York.

Kays, W. M. and London, A. L., 1984, *Compact Heat Exchangers*, third edition, McGraw-Hill, New York.

Moran, M. J., 1982, *Availability Analysis: A Guide to Efficient Energy Use*, Prentice-Hall, Englewood Cliffs, NJ.

Moran, M. J. and Shapiro, H. N., 1995, *Fundamentals of Engineering Thermodynamics*, third edition, Wiley, New York.

Ordoñez, J. C., Vargas, J. V. C. and Bejan, A., 1999, Combined power and refrigeration from a hot stream, *International Journal of Applied Thermodynamics*, Vol. 2, No.2, pp. 49-5